Article

Numerical Model to Analyze the Physicochemical Mechanisms Involved in CO_2 Absorption by an Aqueous Ammonia Droplet

M. I. Lamas Galdo [1,*] , **J. D. Rodriguez García** [2] **and J. M. Rebollido Lorenzo** [3]

1   Escola Politécnica Superior, Universidade da Coruña, 15403 Ferrol, Spain
2   Escola Universitaria Politécnica, Universidade da Coruña, 15405 Ferrol, Spain; de.dios.rodriguez@udc.es
3   IES de Valga, 36645 Xanza, Pontevedra, Spain; navalrebollido@hotmail.com
*   Correspondence: isabel.lamas.galdo@udc.es

Abstract: CO_2 is the main anthropogenic greenhouse gas and its reduction plays a decisive role in reducing global climate change. As a CO_2 elimination method, the present work is based on chemical absorption using aqueous ammonia as solvent. A CFD (computational fluid dynamics) model was developed to study CO_2 capture in a single droplet. The objective was to identify the main mechanisms responsible for CO_2 absorption, such as diffusion, solubility, convection, chemical dissociation, and evaporation. The proposed CFD model takes into consideration the fluid motion inside and outside the droplet. It was found that diffusion prevails over convection, especially for small droplets. Chemical reactions increase the absorption by up to 472.7% in comparison with physical absorption alone, and evaporation reduces the absorption up to 41.9% for the parameters studied in the present work.

Keywords: carbon dioxide; CO_2; absorption; CFD

1. Introduction

The concentration of CO_2 in the atmosphere is increasing at an alarming rate. This trend is causing irreversible climate change, such as atmospheric warming, more extreme weather events, rising sea levels, etc. Since the main anthropogenic source of CO_2 emissions is the combustion of fossil fuels, reducing CO_2 in combustion systems is a crucial task. Mainly, three CO_2 elimination approaches have been developed in the recent years: post-combustion capture, pre-combustion capture, and oxy-combustion. Compared to the other two technologies, post-combustion capture is easier to implement in existing power plants. It is currently the most mature process for CO_2 capture [1,2] and has also been successfully applied for SO_x from many years [3–6].

Among the most commonly used post-combustion methods for CO_2 elimination are membrane separation, cryogenic separation, adsorption, physical absorption, and chemical absorption. In membrane separation, membranes allow only CO_2 to pass through, and other flue gas components are excluded. Cryogenic separation is based on CO_2 separation by condensation. That is, flue gas containing CO_2 is cooled to condensation and then separated from other gases. Adsorption is a physical process that involves attaching gas or liquid to a solid surface. Physical absorption involves CO_2 absorption into the solvent, while in chemical absorption CO_2 reacts with a solvent. Typical solvents are amines, aminoacids, alkalonanimes (DEA, MEA, MDEA, etc.), ammonia, alkalis (NaOH, K_2CO_3, Na_2CO_3, etc.), piperazine, etc. Chemical absorption is widely employed due to higher selectivity and capture efficiencies, even at low CO_2 concentrations [7–11].

Alkalis are the most representative solvents for chemical absorption. Both strong alkaline solutions, such as KOH or NaOH, and weak ones, such as alcohol amines or ammonia, are employed on a wide scale. The main disadvantages of strong alkaline solutions are the corrosion caused to the equipment and difficulties on the resourcelization of the products. Alcohol amines have also been widely used. However, a great deal of

Int. J. Environ. Res. Public Health **2021**, *18*, 4119

2 of 16

energy is needed for regeneration and may also cause corrosion to the equipment. In recent years, ammonia has been a popular alternative; it has high absorption efficiency and absorption capacity, as well as low energy requirements for absorbent regeneration. Moreover, resources are widely distributed. Another advantage is that ammonia can also reduce other pollutants, including SO_2 and NO_x [12–16].

Chemical absorbers include, among others, bubble reactors, sieve-plate towers, packed bed scrubbers, magnetic stirred tanks, and spray towers. Of these, spray towers are the most widely employed system due to their low pressure drop, simplicity, and low maintenance costs. Several experimental works can be found in the literature about the effect of the liquid and gas flow rate, CO_2 initial concentration, temperature, pressure, etc. Nevertheless, to have a thorough grasp of the CO_2 absorption process, it is necessary to complement experimental measurements with numerical methods. In this regard, one can refer to Javed et al. [17] and Javed et al. [18], who investigated how cyclonic flow enhances CO_2 absorption; or Sadripour et al. [19] and Kavoshi et al. [20], who analyzed the effect of the gas temperature, absorbent concentration, and liquid to gas flow rate ratio. The main limitation of these numerical works is that a simulation of the complete spray tower does not provide information about the interior of each droplet. Several papers about single liquid droplets can be found in the literature. One can refer to Choi et al. [21], who analyzed the chemical absorption of CO_2 in a droplet of aqueous NH_3 and developed a correlation to characterize the wall flux as a function of different parameters. Juncu [22] examined the influence of the diffusivity ratio on the mass transfer rate. Wylock et al. [23] studied the interactions between the diffusive and convective mass transports and chemical reactions. Chen et al. [24] compared Selexol, Rectisol, and water as solvents. Pawelski et al. [25] investigated CO_2 absorption into a droplet of a cyclohexanol/methyl chloroacetate/sodium hydroxide solution.

This study focuses on a CFD model for analyzing CO_2 absorption using ammonia as absorbent. Since the main objective is to characterize the governing mechanisms involved, a single droplet was analyzed. The time evolution of the concentration fields, velocity, pressure, and temperature was characterized. This provided information for analyzing the influence of the main physicochemical processes responsible for the rate of absorption, such as diffusion, solubility, convection, and chemical reactions. Additionally, the effect of droplet evaporation was analyzed too. Unlike other numerical models mentioned above, the present work takes into account in the same model both liquid and gas phases, includes the evaporation effect, characterizes the droplet diameter against time, analyzes physical and chemical absorption separately, and studies the effect of both liquid and gas temperatures.

2. Numerical Implementation

The model proposed in the present paper analyzes a single droplet that falls counter-flow with respect to an exhaust gas stream containing CO_2. The computational domain is provided in Figure 1. The domain size was a 15 × 6 droplet radii from the droplet center. It was verified that these dimensions eliminate any potential effect of the outer boundaries on the flow close to the droplet. Several tests were performed to set the most appropriate dimension for the computational domain. The problem was simulated as axisymmetric.
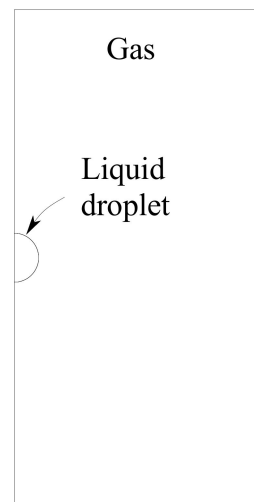
Figure 1. Computational domain.

When viewed in a fixed coordinate system, the droplet and gas move in relation to each other. Modeling this movement requires a large computation domain and, thus, high computation time. An alternative approach is to work with a coordinate system that moves with the droplet. In this case, the droplet is fixed in space and the relative droplet-gas velocity is imposed as inlet and outlet boundary conditions, i.e., the gas flow enters and leaves the computational domain at the relative velocity.

2.1. Chemical Model

At the liquid-gas interface, the gaseous CO_2 dissolves in water and its concentration obeys Henry's law, Equation (1):
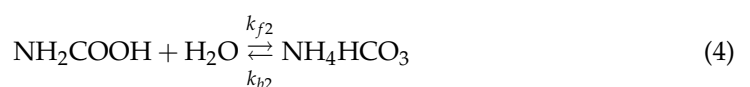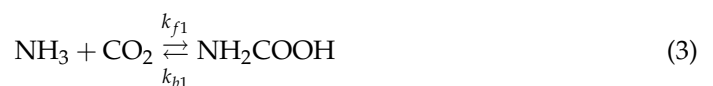
$$C_{CO_2} = p_{CO_2} k_H \tag{1}$$

whereby C_{CO2} is the concentration of CO_2 in the solution, p_{CO2} the partial pressure of CO_2, and k_H the Henry's constant, expressed as, Sander [26]:

$$k_H = k_H^0 e^{\frac{-\Delta H_{\text{soln}}}{R} \left(\frac{1}{T} - \frac{1}{T^0} \right)} \tag{2}$$

whereby k_H^0 is the Henry's constant at the reference state, ΔH_{soln} the solution enthalpy, R the gas constant, T the absolute temperature, and T^0 the reference state temperature. Values of $T^0 = 298.15$ K, $k_H^0 = 0.034$ M/atm, and $-\Delta H_{\text{soln}}/R = 2400$ K were employed [26].

Inside the droplet, the reactions (3)–(6) were assumed [27]. It is worth mentioning that, due to the low temperatures employed in the present work, there should be formation of solid ammonium hydrogen carbonate, NH_4HCO_3, which is a chemical species not considered in this chemical model.

$$NH_3 + CO_2 \underset{k_{b1}}{\overset{k_{f1}}{\rightleftarrows}} NH_2COOH \tag{3}$$

$$NH_2COOH + H_2O \underset{k_{b2}}{\overset{k_{f2}}{\rightleftarrows}} NH_4HCO_3 \tag{4}$$

$$CO_2 + H_2O \underset{k_{b3}}{\overset{k_{f3}}{\rightleftarrows}} H_2CO_3 \tag{5}$$

In these reactions k_{fr} is the forward rate constant for the reaction r and k_{br} the backward rate constant, shown in Table 1 [27,28].

Table 1. Forward and backward constants.

Reaction	Forward Rate Constant	Backward Rate Constant
Equation (3)	$\ln(k_{f1}) = 25.6278 - \frac{44.988}{RT}$	$\ln(k_{b1}) = 0.0078 - \frac{5.3602}{RT}$
Equation (4)	$\ln(k_{f2}) = 2.4078 - \frac{15.851}{RT}$	$\ln(k_{b2}) = 4.6425 - \frac{27.624}{RT}$
Equation (5)	$\ln(k_{f3}) = e^{22.6 - 7799/T} - \ln(C_{H_2O})$	$\ln(k_{b3}) = 30.15 - 8018/T$

2.2. Transport Equations

The level-set method was employed to difference both liquid and gas phases. The conservation of mass and momentum, Equations (6) and (7), were solved for both phases. The energy conservation equation, Equation (8), was also applied. Inside the droplet, the energy equation was solved until the evaporation temperature was reached. Once this temperature is reached it is set as constant and a droplet volume reduction due to phase change is implemented.

$$\nabla \cdot \vec{u} = S_m \tag{6}$$

$$\rho \frac{\partial \vec{u}}{\partial t} + \rho \nabla \cdot (\vec{u}\,\vec{u}) = -\nabla p + \rho \vec{g} - \nabla \cdot \tau + S_{mo} \tag{7}$$

$$\rho c \frac{\partial T}{\partial t} + \rho c \nabla \cdot (\vec{u}\,T) = k\nabla^2 T + S_e \tag{8}$$

whereby u is the velocity, ρ the density, t the time, p the pressure, g the gravitational acceleration, τ the stress tensor, c the specific heat, and k the thermal conductivity. The source term S_m of Equation (6) accounts for the phase change, and is given by [29]:

$$S_m = \left(\frac{1}{\rho_g} - \frac{1}{\rho_l} \right) m \tag{9}$$

whereby $m = \nabla H h(T_e - T_g)/L_v$. The expression $h(T_e - T_g)$ represents the heat transferred between the droplet and gas, and, thus, $h(T_e - T_g)/L_v$ represents the mass transfer per unit area along the interface. T_e is the evaporation temperature, T_g the gas temperature, L_v the latent heat of evaporation, and h the heat transfer coefficient, and is given by [30]:

$$\frac{hD}{k} = 2 + 0.6\mathrm{Re}^{1/2}\mathrm{Pr}^{1/3} \tag{10}$$

whereby D is the droplet diameter, k the thermal conductivity, Re the Reynolds number, and Pr the Prandtl number.

H is the Heaviside function, Equation (11), which was assumed as 0 for the liquid, 1 for the gas, and a value between 0 and 1 along the interface. As mentioned above, the interface was treated using the level set method. This procedure is based on a scalar magnitude, the level set, ϕ, which represents the distance from the interface. The interface corresponds to a zero value of the level set. In the present work, a negative sign of ϕ was adopted for the gas and positive for the liquid.

$$H = \begin{cases} 0 & \text{if } \phi < \varepsilon \\ 1 & \text{if } \phi > \varepsilon \\ (\phi + \varepsilon)/(2\varepsilon) + [\sin(\pi\phi/\varepsilon)]/(2\pi) & \text{if } |\phi| \leq \varepsilon \end{cases} \tag{11}$$

The source term S_{mo} included in the momentum conservation equation, Equation (7), accounts for the effect of surface tension, given by [31]:

$$S_{mo} = \sigma \kappa \nabla H \tag{12}$$

The source term S_e included in the energy conservation equation, Equation (8), accounts for the phase change, and is given by:

$$S_e = L_v m \tag{13}$$

whereby κ is the curvature of the interface, given by:

$$\kappa = -\nabla \cdot \hat{n} \tag{14}$$

whereby $\hat{n}$ is the unit vector in the normal direction of the interface, given by:

$$\kappa = \frac{\nabla \phi}{|\nabla \phi|} \tag{15}$$

In order to take into account the movement of the interface, its propagation was characterized through the following equation:

$$\frac{\partial \phi}{\partial t} + \vec{u}_{\text{int}} \cdot \nabla \phi = 0 \tag{16}$$

whereby $\vec{u}_{\text{int}}$ is the velocity if the interface, which can be obtained through a mass and heat transfer balance at the interface, given by:

$$\vec{m} = \frac{h(T_e - T_g)}{L_v} = \rho(\vec{u}_{\text{int}} - \vec{u}) \tag{17}$$

In order to preserve the characteristic of being distance from the interface, the level set function must be reinitialized at each time step. To this purpose the following equation was employed:

$$\frac{\partial \phi}{\partial \xi} = sign(\phi_0)(1 - |\nabla \phi|) \tag{18}$$

whereby ξ is an artificial time introduced because Equation (18) is a temporal equation which must be solved at each time step, and ϕ_0 is the level set field at the start of each iteration in this artificial time, i.e.,

$$\phi(x, 0) = \phi_0(x) \tag{19}$$

Regarding the chemical treatment, it was assumed that the gas is non-reacting. Nevertheless, in order to take into account species transport in the liquid droplet, the following equation was solved for each ith species:

$$\frac{\partial C_i}{\partial t} + \nabla \cdot (\vec{u} C_i) = \nabla \cdot (D_i \nabla C_i) + R_i \tag{20}$$

whereby C_i is the local concentration of each species, D_i the mass diffusion coefficient, and R_i the net rate of production of species i by the chemical reactions indicated in Equations (3)–(5), given by:

$$R_{\text{NH}_3} = k_{f1} C_{\text{NH}_2\text{COOH}} - k_{b1} C_{\text{NH}_3} C_{\text{CO}_2} \tag{21}$$

$$R_{\text{CO}_2} = k_{f1} C_{\text{NH}_2\text{COOH}} - k_{b1} C_{\text{NH}_3} C_{\text{CO}_2} + k_{f3} C_{\text{H}_2\text{CO}_3} - k_{b3} C_{\text{CO}_2} \tag{22}$$

$$R_{\text{NH}_2\text{COOH}} = k_{f1} C_{\text{NH}_2\text{COOH}} - k_{b1} C_{\text{CO}_2} + k_{f2} C_{\text{NH}_4\text{HCO}_3} - k_{b2} C_{\text{NH}_2\text{COOH}} \tag{23}$$

$$R_{\text{NH}_4\text{HCO}_3} = k_{f2} C_{\text{NH}_4\text{HCO}_3} - k_{b2} C_{\text{NH}_2\text{COH}} \tag{24}$$

$$R_{\text{H}_2\text{CO}_3} = k_{f3} C_{\text{H}_2\text{CO}_3} - k_{b3} C_{\text{CO}_2} \tag{25}$$

Int. J. Environ. Res. Public Health **2021**, *18*, 4119

6 of 16

2.3. Boundary Conditions

As mentioned earlier, a reference frame that moves with the droplet was employed. A free-stream velocity was imposed as inlet and outlet boundary conditions. The drag force tends to reduce the relative velocity between the droplet and gas, and gravity tends to increment it. This was implemented in the numerical model by adjusting the free-stream velocity at each time step. According to this, the acceleration or deceleration is given by:

$$\frac{du_\infty(t)}{dt} = g - \frac{F_{drag}}{\rho_l \pi D^3/6} \tag{26}$$

whereby u_∞ is the free-stream velocity (gas velocity) and F_{drag} the drag force, computed through the following expression:

$$F_{drag} = \frac{C_D A_f \rho_g u_\infty^2}{2} \tag{27}$$

whereby A_f is the reference area (for a sphere $\pi D^2/4$), and C_D the drag coefficient, obtained by the following expression [32]:

$$C_D = \frac{24}{\text{Re}} \left(1 + 0.15\text{Re}^{0.687}\right) \tag{28}$$

Finally, the variation of the free-stream velocity during a time step Δt is:

$$u_\infty(t + \Delta t) = u_\infty(t) + \Delta t \frac{du_\infty(t)}{dt} \tag{29}$$

2.4. CFD Model

The computational mesh is indicated in Figure 2. The grid size is uniform in the tangential direction using $\Delta\theta = 4°$. In the radial direction, the mesh is finer inside the droplet and near the interface. The mesh is made up of tetrahedral elements, and it was modified at the center of the droplet to avoid convergence problems.
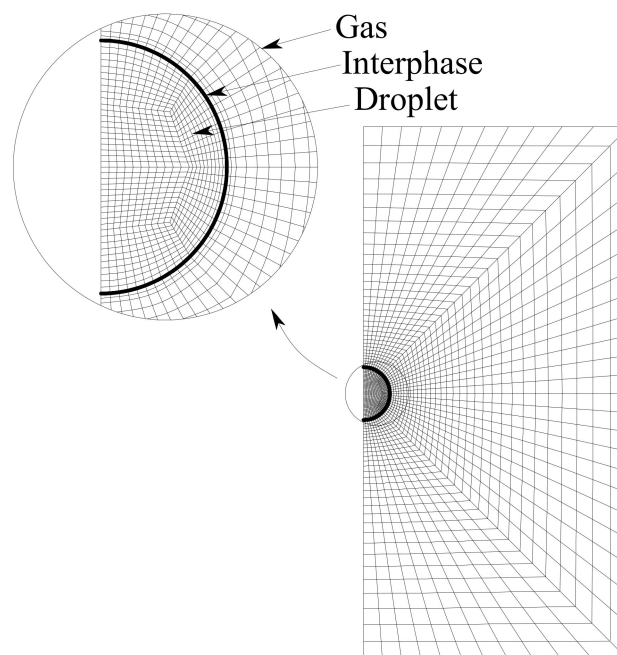

Figure 2. Computational mesh.

Several meshes were tested to verify the adequacy. The model was simulated using the open software OpenFOAM (Open Field Operation and Manipulation, Reading, UK). This software was chosen because the code can be completely manipulated. A new OpenFOAM solver was programmed for the present study using the C++ programming language. OpenFOAM is based on the finite volume method. The pressure-velocity coupling was treated using the PISO (Pressure Implicit Splitting of Operators) procedure. The equations were discretized by QUICK interpolation and the temporal treatment was solved by an implicit method.

2.5. Validation

This evaporation model was validated with experimental results developed elsewhere. Several authors reported data about spherical bubble growing due to evaporation, Plesset and Zwich [33], Scriven [34], Mikic et al. [35], Forster and Zuber [36], etc. These authors developed correlations based on their experimental findings. Figure 3 shows a comparison between these correlations and the results provided by the present numerical model. Particularly, this figure shows the evolution of the radius against time for a spherical bubble of water immersed in a liquid medium 5 °C superheated. As can be seen, this figure shows that the developed numerical based on the level set method model provides reasonably accurate results.
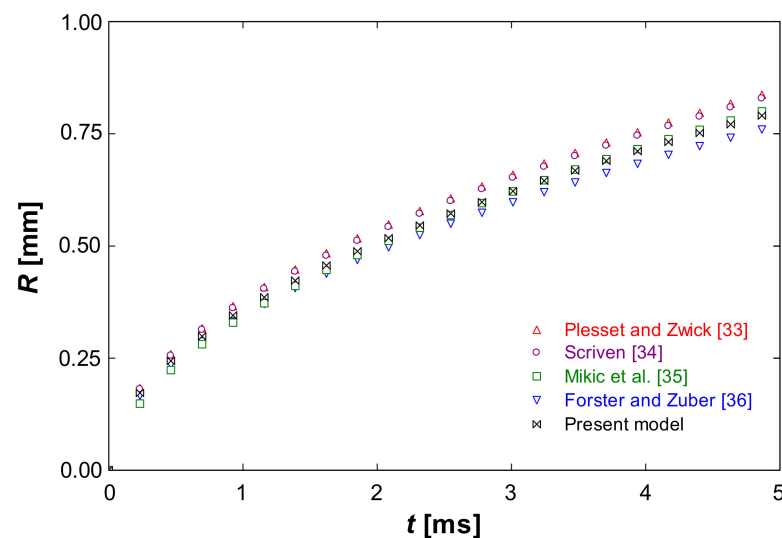

Figure 3. Bubble radius (R) against time (t) applied to a spherical water bubble growing in a 5 °C superheated liquid medium.

Once it was validated, the numerical model was used to study the governing mechanisms responsible for CO_2 absorption, such as diffusion, solubility, convection, chemical reactions, and droplet evaporation. The results are outlined below.

3. Results

All the results showed in this section will be based on velocities corresponding to usual values observed in practical applications [4,5], 2 m/s initial liquid droplet velocity and 0.5 m/s initial gas velocity. This leads to an initial free stream velocity of 2.5 m/s. An initial 15% v/v CO_2 concentration was considered. Figure 4 shows the velocity and concentration of CO_2 at 0.5 and 1 s using 5% initial ammonia concentration, 100 °C initial gas temperature, 5 °C initial liquid temperature, and 1000 μm initial droplet diameter. The concentration is expressed in M, that is, mol/L. Initially, the CO_2 concentration inside the droplet is zero and its concentration at the droplet surface obeys Henry's law. An internal vortex is rapidly induced by the shear stress along the droplet surface and CO_2 is transported to the core. Radial diffusion and chemical reactions also take place. Figure 4

clearly shows that CO_2 is transported from the interface to the core of the droplet due to convection. Once CO_2 is captured into the droplet, it reacts with NH_3. NH_3 is consumed first at the interface and then at the core of the droplet, as can be seen in Figure 5. This figure illustrates the NH_3 concentration at 0.5 and 1 s.
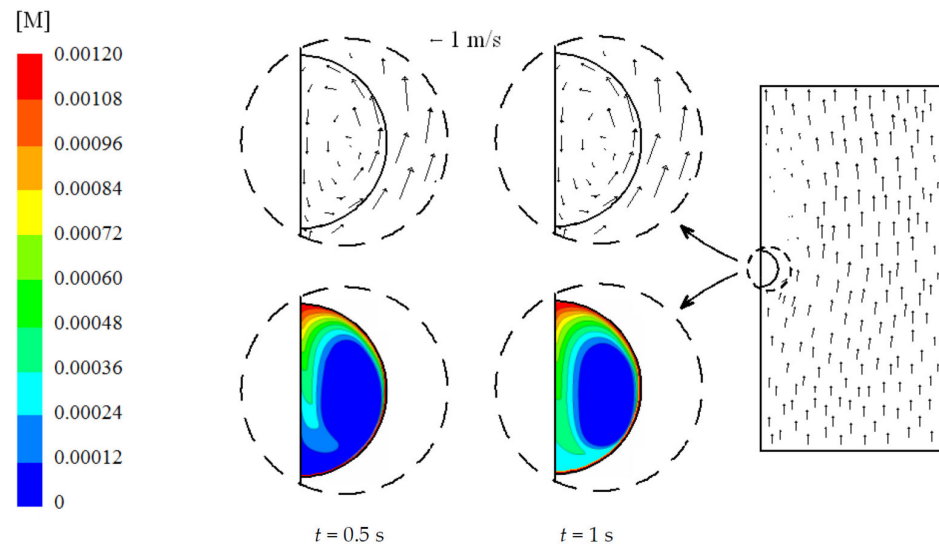

Figure 4. Velocity field and concentration of CO_2 for time (t) 0.5 and 1 s. 5% initial ammonia concentration, 100 °C initial gas temperature, 5 °C initial liquid temperature, and 1000 μm initial droplet diameter.
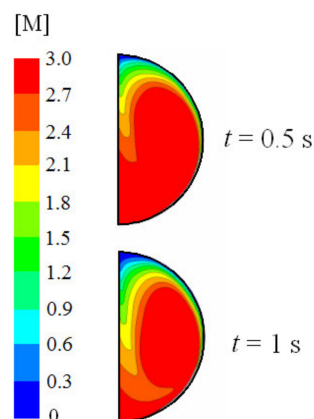
Figure 5. Concentration of NH_3 for time (t) 0.5 and 1 s. 5% initial ammonia concentration, 100 °C initial gas temperature, 5 °C initial liquid temperature, and 1000 μm initial droplet diameter.

3.1. Effect of Convection and Diffusion under Several Initial Droplet Diameters

Figure 6 shows the droplet diameter against time for 1000, 500, and 100 μm initial diameters. As expected, all droplets experience a reduction in their diameters due to the evaporation phenomena implemented in the model. All droplets remained practically spherical during the entire simulation due to the importance of the surface tension in comparison with the inertial force. Other authors also observed spherical shapes for droplets falling in a gas phase when the diameters are less than 1000 μm approximately [23]. Elperin and Fomykh [37] observed spherical shapes until 1100 μm diameter. Akbar [38] mentioned a 1000 μm limit for limestone droplets, and beyond this value they observed deformations of the droplet and oscillation at the interface. This limit was also mentioned in the numerical study of Amokrane and Caussade [39]. Clift et al. [40] reported that water droplets smaller than 1000 μm falling in air can be considered as rigid spheres.
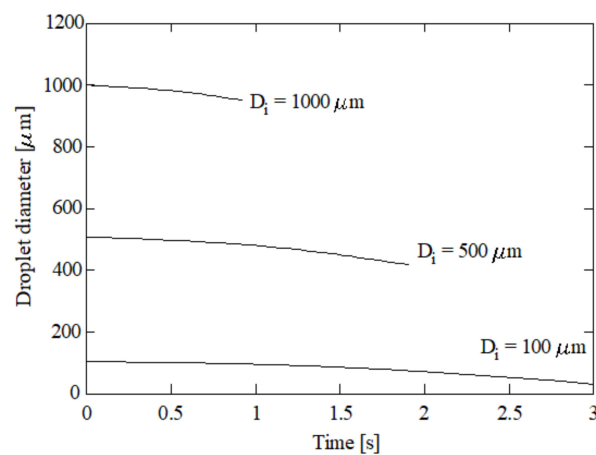
Figure 6. Droplet diameter against time for several initial diameters. 5% initial ammonia concentration, 100 °C initial gas temperature, and 5 °C initial liquid temperature.

The droplet velocity and position for these initial diameters can be found in Figures 7 and 8 respectively. Figures 6–8 correspond to 15% initial CO_2 concentration, 5% initial ammonia concentration, 100 °C initial gas temperature, and 5 °C initial liquid temperature. As scrubber length, a typical value of 2000 mm [4,5] was assumed. As can be seen in Figure 8, the larger droplet, with an initial diameter of 1000 μm, has a residence time of 0.87 s. This is the time needed to reach 2000 mm in length assumed as height of the scrubber. The droplet with initial diameter of 500 μm needs 1.81 s to reach a 2000 mm length and the droplet with a 100 μm diameter reverses its trajectory. That is, the weight is small enough for the droplet to be displaced upwards instead of downwards. As expected, lower diameters correspond to lower velocities. As shown in Equation (26), two effects are responsible for the droplet trajectory: gravity and drag. Larger droplets are associated with high gravity forces (high weights) and, thus, to high velocities. Nevertheless, as the droplet diameter is reduced, i.e., the weight is reduced, gravity plays a lesser role and the velocity tends to decay. As can be seen in Figure 7, the terminal velocities for the droplets with initial diameters of 1000, 500, and 100 μm are 2.38, 0.81, and −0.19 m/s respectively. The largest droplets, corresponding to 1000 μm, increments its initial velocity due to their important weights, while the other droplets, 500 and 100 μm initial diameters, reduce their initial velocity due to their reduced weight.
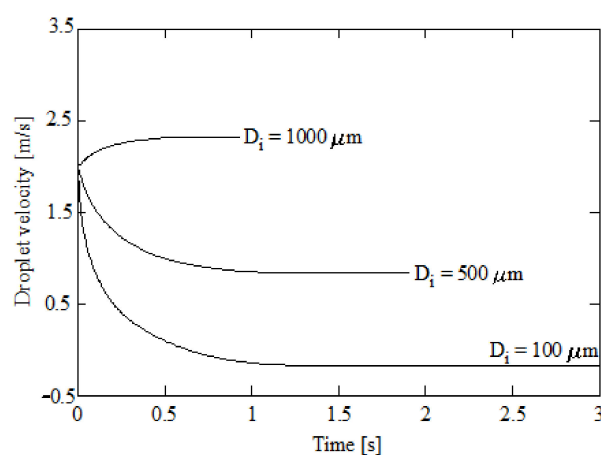

Figure 7. Droplet velocity against time for several initial diameters; 5% initial ammonia concentration, 100 °C initial gas temperature, and 5 °C initial liquid temperature.
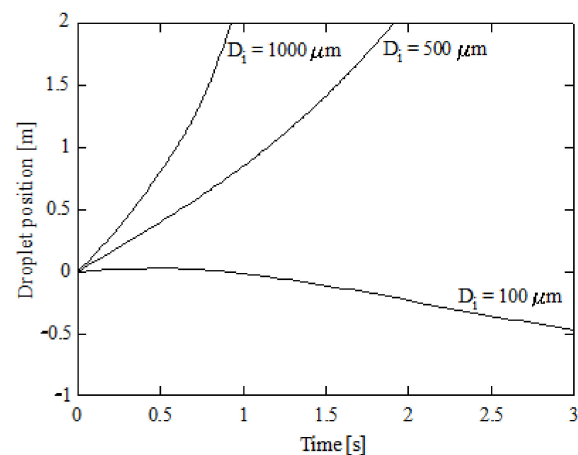
Int. J. Environ. Res. Public Health **2021**, 18, 4119

10 of 16

Figure 8. Droplet position against time for several initial diameters; 5% initial ammonia concentration, 100 °C initial gas temperature, and 5 °C initial liquid temperature.

The quantity of carbon absorbed by each droplet is given in Figure 9. Here, the droplet with an initial diameter of 100 μm was discarded due to the inversion of its trajectory. As can be seen, larger droplets are associated with higher carbon absorption even though their residence time is lower. Nevertheless small droplets are associated with lower carbon absorption.
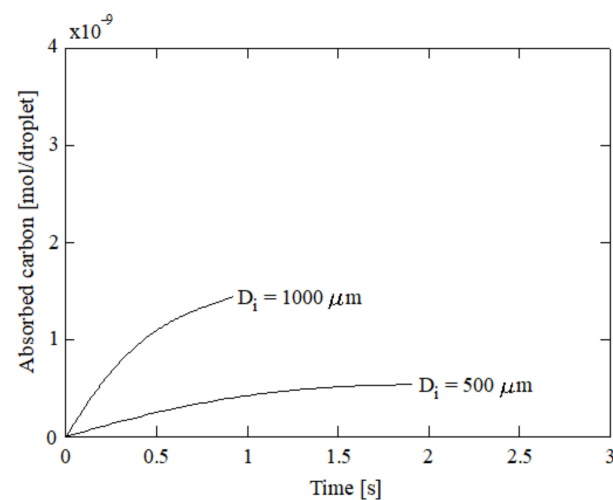

Figure 9. Carbon absorbed by a droplet for several initial diameters; 5% initial ammonia concentration, 100 °C initial gas temperature, and 5 °C initial liquid temperature.

Figure 10a,b provide the concentration of CO_2 for droplets with initial diameters of 1000 and 500 μm respectively between 0.5 and 3 s (in case it was possible for the residence time to be 3 s. As mentioned earlier, the droplets with a 1000 μm diameter reach the lower part of the column before 3 s elapse). As can be seen, the droplet with the smaller diameter, 500 μm, presents a distribution of CO_2 dominated by diffusion since the time evolution of the concentration field is very close to what would be observed in a purely diffusive process: it is almost spherically symmetric. The droplet with the larger initial diameter, 1000 μm, presents a distribution of CO_2 in a first stage dominated by convection with a highly asymmetric profile. For this droplet, initially CO_2 is transported by convection in the periphery, depleting the diffusion concentration boundary layer and enhancing mass transfer. After that, it penetrates the droplet due to diffusion.
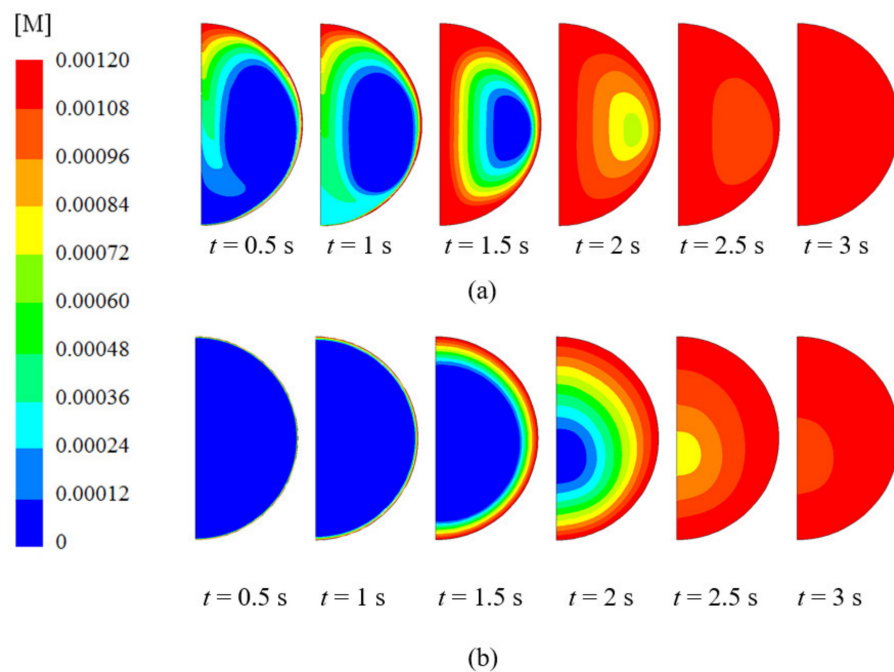
Figure 10. Concentration of CO_2 against time (t); (**a**) 1000 μm initial diameter; (**b**) 500 μm initial diameter. 5% initial ammonia concentration, 100 °C initial gas temperature, and 5 °C initial liquid temperature.

3.2. Effect of Physical and Chemical Absorption

It is interesting to analyze in detail the effect of chemical dissociation. To this end, Figure 11 compares physical and chemical absorption, that is, in the absence and presence of chemical dissociation, respectively, at a 100 °C initial gas temperature, 5 °C initial liquid temperature, and 1000 μm initial diameter. The absorbed carbon was computed as the sum of moles of CO_2, NH_2COOH, and H_2CO_3. As can be seen, initially the four curves are extremely similar since CO_2 is the main species in the droplet. As time progresses, the chemical absorption becomes more intense than the physical one due to the formation of NH_2COOH and H_2CO_3. The absorption of carbon from the flue gas is increased. In the case of 12% initial NH_3 concentration, an absorption increase of 472.7% over physical absorption was obtained. Another conclusion that can be obtained from Figure 11 is that chemical dissociation prolongs the carbon capture process because more time is needed to reach the saturation state.
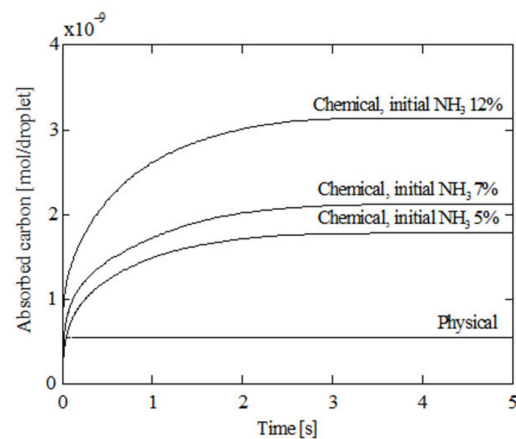

Figure 11. Absorbed carbon under physical and chemical absorption; 5% initial ammonia concentration, 100 °C initial gas temperature, 5 °C initial liquid temperature, and 1000 μm initial diameter.

3.3. Effect of Evaporation and Temperature

It is interesting to analyze the effect of evaporation on the absorption process. Evaporation is closely related to temperature. In practical applications, the liquid can be easily injected at ambient temperature but the gas resulting from combustion remains at a high temperature. An increase in the temperature facilitates the forward reactions of Equations (3)–(5) and, thus, NH_4HCO_3 and H_2CO_3 formation, leading to improve carbon absorption. Nevertheless, a rise in temperature increases the interface temperature and the Henry's constant is reduced. This lowers the amount of CO_2 at the interface and, with it, the absorption process. Figure 12 shows the liquid and gas temperature against time at 5% initial ammonia concentration, 100 °C initial gas temperature, 5 °C initial liquid temperature, and 1000 μm initial diameter. As can be seen, the liquid is heated and the gas is cooled once they are in contact. The variation in the liquid temperature is more pronounced than that in the gas temperature since water has a higher heat capacity than gas. The average interface temperature against time is represented in Figure 13 (in case it was possible for the residence time to be 3 s).
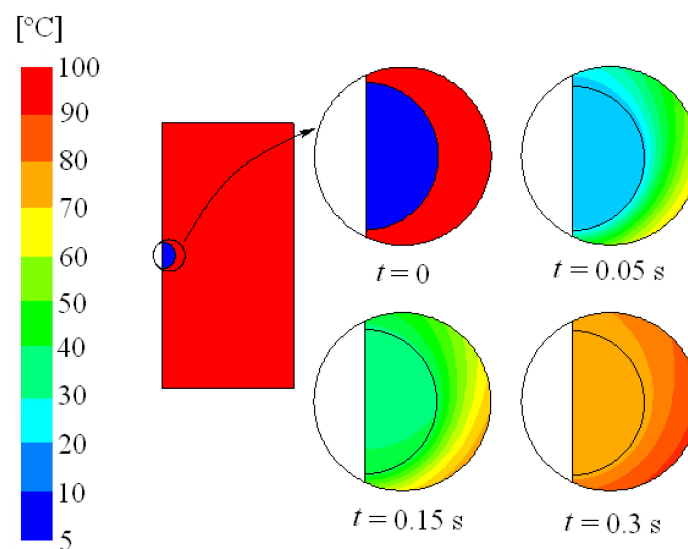

Figure 12. Temperature field for time (t) 0, 0.05, 0.15, and 0.3 s; 5% initial ammonia concentration, 100 °C initial gas temperature, 5 °C initial liquid temperature, and 1000 μm initial diameter.
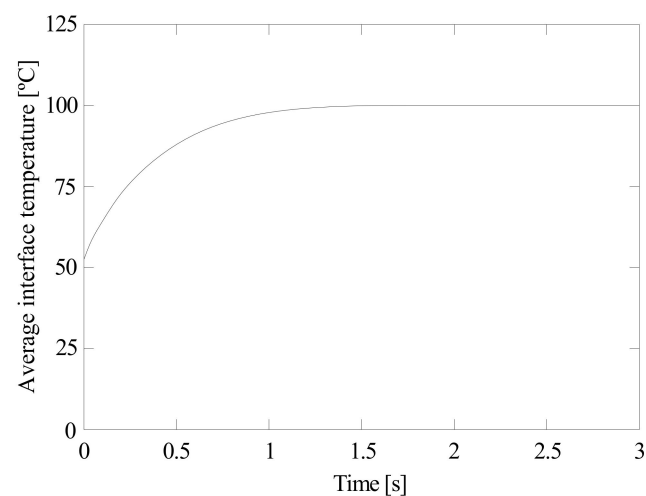

Figure 13. Average interface temperature. 5% initial ammonia concentration, 100 °C initial gas temperature, 5 °C initial liquid temperature, and 1000 μm initial diameter.

Int. J. Environ. Res. Public Health **2021**, *18*, 4119

13 of 16

Figure 14 shows the carbon absorbed by a droplet against time at a 5% initial ammonia concentration, 5 °C initial liquid temperature, and 1000 µm initial diameter. Three gas temperatures were represented: 100, 125, and 150 °C. As can be seen, the carbon absorption decreases with the gas temperature due to a reduction in the Henry's constant. Previous works also revealed similar trends using ammonia [8] and other solvents such as DEA and AEEA [41]. Another effect that decreases carbon absorption is evaporation. If the gas temperature is increased, the droplet's diameter is reduced due to evaporation. Figure 14 shows the absorbed carbon for 150 °C than 100 °C. As can be seen, higher temperatures promote higher residence times due to lower velocities, but the droplet diameter is reduced and, thus, the CO_2 absorption. In Figure 15, the droplet diameter against time is provided for 100, 125, and 150 °C. As can be seen, the droplet diameter experiences a considerable reduction with the gas temperature. The main consequence is a reduction in the absorbed carbon. Particularly, a 48.7% reduction in the absorbed carbon was obtained from 100 to 150 °C. The simulations were repeated using a constant diameter and the reduction in carbon absorption was 41.9%, which confirms the role played by evaporation.
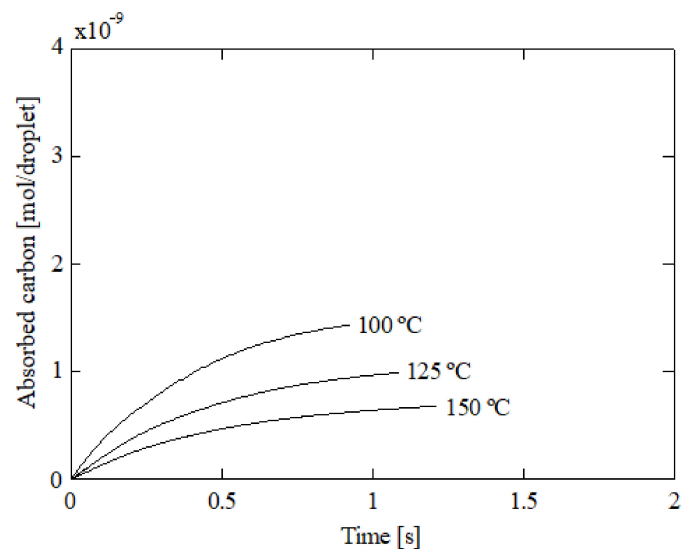

Figure 14. Absorbed carbon by a droplet for several initial gas temperatures; 5% initial ammonia concentration, 5 °C initial liquid temperature, and 1000 µm initial diameter.
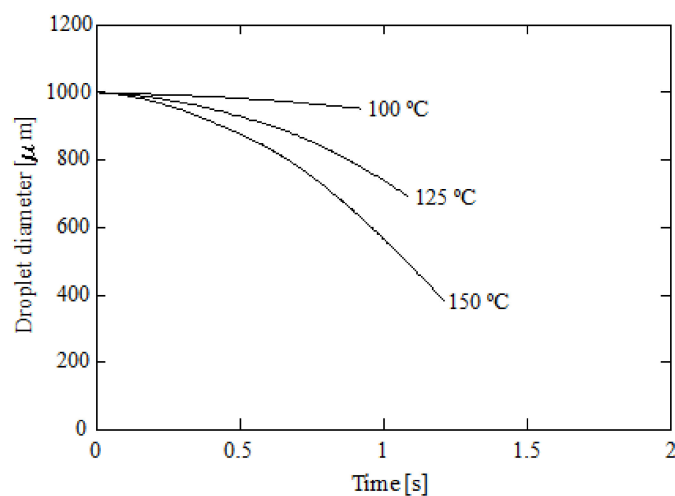

Figure 15. Droplet diameter against time for several initial gas temperatures; 5% initial ammonia concentration, 5 °C initial liquid temperature, and 1000 µm initial diameter.

Int. J. Environ. Res. Public Health **2021**, *18*, 4119

14 of 16

The influence of the liquid temperature is illustrated in Figure 16, which shows the carbon absorption corresponding to a 5, 20, and 40 °C liquid temperature. In this figure, it can be seen that the carbon absorption is higher for 20 °C and lower for 40 °C.
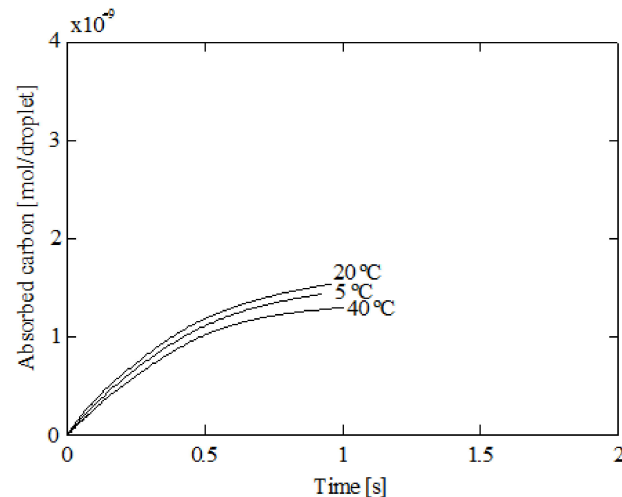

Figure 16. Absorbed carbon by a droplet for several initial liquid temperatures; 5% initial ammonia concentration, 100 °C initial gas temperature, and 1000 μm initial diameter.

4. Conclusions

This work presents a numerical analysis to study CO_2 capture by ammonia. Aqueous ammonia was employed as absorbent due to its high absorption capacity, low energy requirement for regeneration, and good inoxidability. The results obtained can be channeled to the improvement of equipment operation and efficiency such as absorption and stripper columns, as well as the process of regeneration of absorbents.

A single droplet was studied. The analysis of the time evolution of the species, velocity and temperature provided information about the governing psychochemical phenomena, such as diffusion, solubility, convection, chemical reactions, and evaporation. It was found that diffusion prevails over convection, especially for small droplets. Convection is important in the initial instants of the process. Chemical reactions increment the absorption rate up to 472.7% in comparison with physical absorption alone for the parameters analyzed in the present work. Chemical reactions enhance the mass transfer and delay the saturation state. For the parameters studied, it was found that the droplet evaporation reduces the absorption rate by up to 41.9%. The flue gas temperature has a considerable influence on both evaporation and absorption.

It is worth noting that the main drawback of the present work is that it neglects ammonia evaporation, since this will evaporate much faster than water and, thus, its concentration is affected. Ammonia might escape from the solution before the reaction with CO_2, and this phenomenon will be object of analysis in future works. Another areas for future research work will be analyzing larger droplets and the effect of the exhaust gas humidity.

Author Contributions: Conceptualization: M.I.L.G., J.D.R.G., and J.M.R.L.; methodology: M.I.L.G., J.D.R.G., and J.M.R.L.; validation: M.I.L.G.; formal analysis: M.I.L.G., J.D.R.G., and J.M.R.L.; investigation: M.I.L.G., J.D.R.G., and J.M.R.L.; resources: M.I.L.G., J.D.R.G., and J.M.R.L.; writing—original draft preparation: M.I.L.G.; writing—review and editing: M.I.L.G., J.D.R.G., and J.M.R.L. All authors have read and agreed to the published version of the manuscript.

Institutional Review Board Statement: Not applicable.

Informed Consent Statement: Not applicable.

Conflicts of Interest: The authors declare no conflict of interest.

References

1. Leung, D.Y.C.; Caramanna, G.; Maroto-Valer, M.M. An overview of current status of carbon dioxide capture and storage technologies. *Renew. Sustain. Energy Rev.* **2014**, *39*, 426–443. [CrossRef]
2. Wang, C.; Lawal, M.; Stephenson, A.; Sidders, P.; Ramshaw, J. Post-combustion CO2 capture with chemical absorption: A state-of-the-art-review. *Chem. Eng. Res. Des.* **2011**, *89*, 1609–1624. [CrossRef]
3. Ammar, N.R.; Seddiek, I.S. Eco-environmental analysis of ship emission control methods: Case study RO-RO cargo vessel. *Ocean Eng.* **2017**, *137*, 166–173. [CrossRef]
4. Lamas, M.I.; Rodríguez, C.G.; Rodríguez, J.D.; Telmo, J. Numerical model of SO2 scrubbing with seawater applied to marine engines. *Polish Marit. Res.* **2016**, *23*. [CrossRef]
5. Lamas, M.I.; Rodriguez, C.G. CFD Model to Analyze SO2 Absorption in a Seawater Droplet. *Int. J. Marit. Eng.* **2019**, *161*, 335–444. [CrossRef]
6. Puškár, M.; Kopas, M.; Sabadka, D.; Kliment, M.; Šoltésová, M. Reduction of the Gaseous Emissions in the Marine Diesel Engine Using Biodiesel Mixtures. *J. Mar. Sci. Eng.* **2020**, *8*, 330. [CrossRef]
7. Park, S.W.; Lee, J.W.; Choi, B.S.; Lee, J.W. Absorption of carbon dioxide into non-aqueous solutions ofN-methyldiethanolamine. *Korean J. Chem. Eng.* **2006**, *23*, 806–811. [CrossRef]
8. Lee, D.H.; Choi, W.J.; Moon, S.J.; Ha, S.H.; Kim, I.G.; Oh, K.H. Characteristics of absorption and regeneration of carbon dioxide in aqueous 2-amino-2-methyl-1-propanol/ammonia solutions. *Korean J. Chem. Eng.* **2008**, *25*, 279–284. [CrossRef]
9. Glasscock, D.A.; Critchfield, J.E.; Rochelle, G.T. CO2 absorption/desorption in mixtures of methyldiethanolamine with monoethanolamine or diethanolamine. *Chem. Eng. Sci.* **1991**, *46*, 2829–2845. [CrossRef]
10. Versteeg, C.F.; Kuipers, J.A.M.; Van Beckum, F.P.H.; Van Swaaij, W.P.M. Mass transfer with complex reversible chemical reactions—II. parallel reversible chemical reactions. *Chem. Eng. Sci.* **1990**, *45*, 183–197. [CrossRef]
11. Freeman, S.A.; Dugas, R.; Van Wagener, D.; Nguyen, T.; Rochelle, C.T. Carbon dioxide capture with concentrated, aqueous piperazine. *Energy Procedia* **2009**, *1*, 1489–1496. [CrossRef]
12. Larbi, N.; Bessrour, J. Measurement and Simulation of Pollutant Emissions from Marine Diesel Combustion Engine and Their Reduction by Ammonia Injection. *Adv. Mech. Eng.* **2009**, *1*, 459813. [CrossRef]
13. Puškár, M.; Kopas, M.; Puškár, D.; Lumnitzer, J.; Faltinová, E. Method for reduction of the NOX emissions in marine auxiliary diesel engine using the fuel mixtures containing biodiesel using HCCI combustion. *Mar. Pollut. Bull.* **2018**, *127*, 752–760. [CrossRef]
14. Píštěk, V.; Kučera, P.; Fomin, O.; Lovska, A. Effective Mistuning Identification Method of Integrated Bladed Discs of Marine Engine Turbochargers. *J. Mar. Sci. Eng.* **2020**, *8*, 379. [CrossRef]
15. Varbanets, P.R.; Fomin, O.; Pistek, V.; Klymenko, V.; Minchev, D.; Khrulev, A.; Zalozh, V.; Kucera, P. Acoustic method for estimation of marine low-speed engine turbocharger parameters. *J. Mar. Sci. Eng.* **2021**, *9*, 321. [CrossRef]
16. Homišin, J.; Kaššay, P.; Urbanský, M.; Puškár, M.; Grega, R.; Krajňák, J. Electronic Constant Twist Angle Control System Suitable for Torsional Vibration Tuning of Propulsion Systems. *J. Mar. Sci. Eng.* **2020**, *8*, 721. [CrossRef]
17. Javed, K.H.; Mahmud, T.; Purba, E. Enhancement of Mass Transfer in a Spray Tower Using Swirling Gas Flow. *Chem. Eng. Res. Des.* **2006**, *84*, 465–477. [CrossRef]
18. Javed, K.H.; Mahmud, T.; Purba, E. The CO_2 capture performance of a high-intensity vortex spray scrubber. *Chem. Eng. J.* **2010**, *162*, 448–456. [CrossRef]
19. Sadripour, M.; Rahimi, A.; Hatamipour, M.S. CFD Modeling and Experimental Study of a Spray Dryer Performance. *Chem. Prod. Process Model.* **2014**, *9*, 15–24. [CrossRef]
20. Kavoshi, L.; Rahimi, A.; Hatamipour, M.S. CFD modeling and experimental study of carbon dioxide removal in a lab-scale spray dryer. *Chem. Eng. Res. Des.* **2015**, *98*, 157–167. [CrossRef]
21. Choi, M.; Cho, M.; Lee, J.W. Empirical formula for the mass flux in chemical absorption of CO2 with ammonia droplets. *Appl. Energy.* **2016**, *164*, 1–9. [CrossRef]
22. Juncu, G. Conjugate mass transfer to a spherical drop accompanied by a second-order chemical reaction inside the drop. *Int. J. Heat Mass Transf.* **2002**, *45*, 3817–3829. [CrossRef]
23. Wylock, C.; Colinet, P.; Haut, B. Gas absorption into a spherical liquid droplet: Numerical and theoretical study. *Chem. Eng. J.* **2012**, *207*, 851–864. [CrossRef]
24. Chen, W.H.; Tsai, M.H.; Hung, C.I. Numerical prediction of CO2 capture process by a single droplet in alkaline spray. *Appl. Energy* **2013**, *109*, 125–134. [CrossRef]
25. Pawelski, A.; Jeon, S.J.; Hong, W.H.; Paschedag, A.R.; Kraume, M. Interaction of a homogeneous chemical reaction and mass transfer in a single moving droplet. *Chem. Eng. Sci.* **2013**, *104*, 260–268. [CrossRef]

26. Sander, R. Henry's Law Constants. In *NIST Chemistry Webbook, SRD 69*; Linstrom, P.J., Mallard, W.G., Eds.; National Institute of Standards and Technology: Gaithersburg, MD, USA, 2005.

27. Wilcox, J. Introduction to Carbon Capture. In *Carbon Capture*; Springer: New York, NY, USA, 2012; pp. 1–34.

28. Nilsson, J. Development of a Model for Wet Scrubbing of Carbon Dioxide by Chilled Ammonia. Ph.D. Thesis, Lund University, Lund, Sweden, 2009.

29. Sim, J.; Im, H.G.; Chung, S.H. A computational study of droplet evaporation with fuel vapor jet ejection induced by localized heat sources. *Phys. Fluids* **2015**, *27*, 053302. [CrossRef]

30. Ranz, W.R.; Marshall, W.E. Evaporation from drops. *Parts I II Chem. Eng. Prog.* **1952**, *48*, 141–146.

31. Brackbill, J.; Kothe, D.; Zemach, C. A continuum method for modeling surface tension. *J. Comput. Phys.* **1992**, *100*, 335–354. [CrossRef]

32. Seinfeld, J.H. *Atmospheri Chemistry and Physics of Air Pollution*; Willey: New York, NY, USA, 1986.

33. Plesset, M.S.; Zwick, S.A. The growth of vapor bubbles in superheated liquids. *J. Appl. Phys.* **1954**, *25*, 493–500. [CrossRef]

34. Scriven, L.E. On the dynamics of phase growth. *Chem. Eng. Sci.* **1959**, *10*, 1–13. [CrossRef]

35. Mikic, B.; Rohsenow, W.; Griffith, P. On bubble growth rates. *Int. J. Heat Mass Transf.* **1970**, *13*, 657–666. [CrossRef]

36. Forster, H.K.; Zuber, N. Growth of a vapor bubble in a superheated liquid. *J. Appl. Phys.* **1954**, *25*, 474–478. [CrossRef]

37. Elperin, T.; Fominykh, A. Conjugate mass transfer during gas absorption by falling liquid droplet with internal circulation. *Atmos. Environ.* **2005**, *39*, 4575–4582. [CrossRef]

38. Akbar, M.K.; Yan, J.; Ghiaasiaan, S.M. Mechanism of gas absorption enhancement in a slurry droplet containing reactive, sparingly soluble microparticles. *Int. J. Heat Mass Transf.* **2003**, *46*, 4561–4571. [CrossRef]

39. Amokrane, H.; Caussade, B. Gas absorption into a moving spheroidal water drop. *J. Atmos. Sci.* **1999**, *56*, 1808–1829. [CrossRef]

40. Clift, R.; Grace, J.; Weber, M. *Bubbles, Drops and Particles*; Dover Publications: Mineola, NY, USA, 1978.

41. Bajpai, A.; Mondal, M.K. Equilibrium solubility of CO2 in aqueous mixtures of DEA and AEEA. *J. Chem. Eng. Data* **2013**, *58*, 1490–1495. [CrossRef]